

The Crushing Distribution Morphology of a Single Particle Subjected to Rotary Impact

Canhui Wu, Limei Zhao,* and Zhen Cao



Cite This: *ACS Omega* 2024, 9, 31464–31476



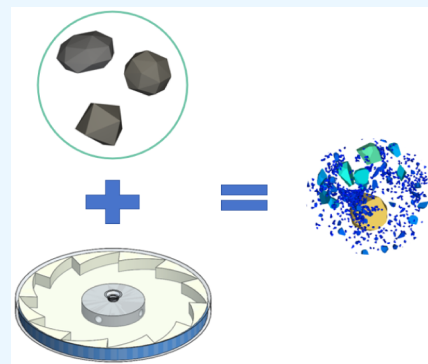
Read Online

ACCESS |

Metrics & More

Article Recommendations

ABSTRACT: In a vertical shaft impact crusher, the particle crushing process is extraordinarily complex, and the particle shape significantly influences the size distribution of the crushed product. To quantify the crushing behavior of particles more accurately and thus reveal the crushing mechanism of the crusher, an analytical approach is suggested for characterizing the crushing distribution of particles subjected to rotational impact. First, according to the working principle of vertical shaft impact crusher, a rotary impact tester was designed, and the cumulative damage model of particles under repetitive impact was established based on the theory of fracture mechanics, based on which the simulation model of single-particle rotary impact tester was constructed. Then, seven distinct particle shapes were established based on the particle shapes observed during the crusher's actual production. Finally, an investigation was conducted using the simulation model to examine the impact of various rotor velocities and particle shapes on the macroscopic mechanical properties and crushing distribution attributes of single-particle crushing. In the single-particle rotary impact crushing experiments, the findings indicated that the particle crushing transpired at the site of contact with the anvil. The particle size distribution of subparticles generated through the crushing with distinct particle shapes all exhibit single-peak characteristics as rotor speed increases. The magnitude of the peak value progressively escalates in tandem with the rotor speed increase. Furthermore, as the rotor speed increases, so do the cumulative mass distribution and the maximum continuous crushing cumulative mass. When the horizontal aspect ratio of the particles is $V < 1$ and $V > 1$, the crushing effect of the particles is poor at the same rotational speed; the curve of the maximum continuous crushing degree has an inverted "V" shape. The crushing effect of the particles improves as their edges become progressively sharper, and the maximum continuous crushing degree of the particles increases as the edge sharpness of the particles advances.



1. INTRODUCTION

Sand, a critical raw material in the infrastructure sector, is usually obtained by crushing rock materials in vertical shaft impact crushers,¹ the primary crushing apparatus utilized in the production of sand and gravel. Various factors, including rotor speed significantly influence the crushing process of this equipment. Furthermore, the shape of the material particles is diverse and unpredictable, which presents a challenge in conducting crushing experiments to investigate the crusher's mechanism.^{2–5} Effectively quantifying the crushing behavior of material particles is the key to analyzing the crusher crushing mechanism. As a result, an in-depth examination of the impact crushing properties of particles is crucial for elucidating the crushing mechanism of the crusher, thereby optimizing the structure of the crusher and enhancing its crushing efficiency.⁶

At present, the majority of research devoted to the impact-crushing properties of particles is categorized as either multiparticle impact crushing or single-particle impact crushing.⁷ One approach is multiparticle impact crushing, which investigates the collective crushing effect of a group of particles. However, this method fails to capture the intricate crushing process of individual particles and presents challenges

in elucidating their specific crushing characteristics. As a result, single-particle impact crushing experiments have emerged as the predominant method for studying the crushing characteristics of particles.^{8,9} Current investigations of the impact-crushing properties of individual particles rely primarily on the pendulum impact test¹¹ and the falling weight impact test.¹⁰ Nevertheless, the experiments above utilized bidirectional passive compression to crush the particles, as all particles were supported. However, in the vertical shaft impact crusher, the particles fall into the distributing cone of the high-speed rotor by gravity and are evenly dispersed by the distributing cone to each guide plate. Particles on the guide plate accelerate to the outer edge of the rotor under the effect of centrifugal force, are thrown out at high speed at the end of the guide plate, and

Received: January 31, 2024

Revised: July 1, 2024

Accepted: July 2, 2024

Published: July 11, 2024



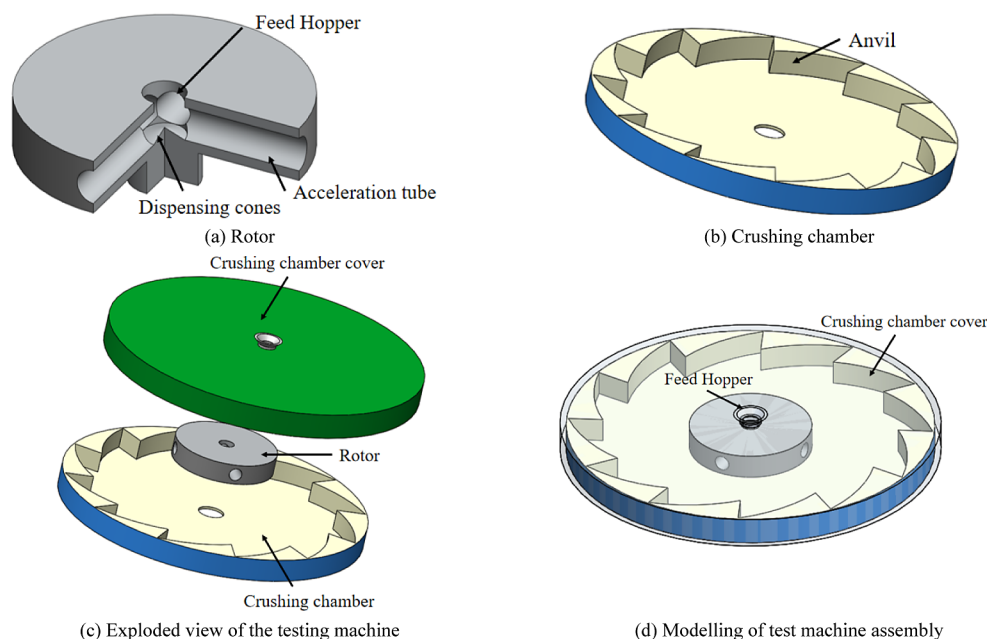


Figure 1. Geometric model of the rotary impact tester.

finally crush with the anvil by impact collision.^{2–5} As can be seen, the particle's unidirectional impact is primarily responsible for crushing the particles in the crusher. As a result, the crushing distribution characteristics of particles in a vertical shaft impact crusher cannot be precisely analyzed, as the crushing principles of the falling weight impact test and the pendulum impact test on particles are inconsistent with those of the vertical shaft impact crusher.¹² As a result, designing a kind of testing machine to make the particle rotationally accelerated and then unidirectionally impacted and crushed, in conjunction with the crushing principle of a vertical shaft impact crusher, is of critical reference importance for the investigation of the crushing mechanism of vertical shaft impact crushers.

In terms of investigation of the properties of impact crushing on individual particles, Tavares et al. utilized fracture damage mechanics to examine the crushing properties of particles subjected to varying impact energies and developed a cumulative damage crushing model of particles.^{13–15} Hagelman et al. performed compression crushing tests on spherical and angular-edged particles, and the results indicated that the shape of the material affected the crushing stresses during the particle crushing process.¹⁶ In their investigation, Miao et al. examined the dispersion pattern of various ellipsoidal limestone particles after impact crushing. The findings revealed that the shape and impact energy of the particles during the impact procedure significantly influence the postcrushing distribution pattern.¹⁷ The crushing effect of particles increases as the impact velocity rises, and the findings of Zheng et al. regarding the crushing behavior of particles of various shapes revealed that the impact velocity has a direct correlation with the particle shape. Objects exhibit a more intricate collision behavior in comparison to spherical objects.¹⁸ In addition, Wang et al. investigated the crushing characteristics of individual particles through uniaxial compression tests. Their findings revealed that particles exhibiting a greater degree of sphericity were more susceptible to crushing under explosion modes of higher intensity. Conversely, particles with a lesser

degree of sphericity were more likely to be crushed at lower intensities.¹⁹ Although considerable progress has been made in the study of the crushing behavior of single particles, current research focuses primarily on the experimental method of two-way extrusion of material particles and the shape of the particles is distinct ellipsoid shapes. The particle shape and crushing principle of ellipsoidal particles are significantly dissimilar to those utilized in vertical shaft impact crushers. Furthermore, experimental methods make it difficult to observe the crushing process of individual particles due to equipment limitations.²⁰ Hence, to surmount the constraints of empirical investigation and gain a more comprehensive understanding of the evolution mechanism and overall mechanical characteristics of the particle crushing process.^{21–23}

The study used the discrete element method to investigate the crushing characteristics of particles which can discretize the complete particle crushing process, enabling a frame-by-frame analysis of the particle crushing procedure.^{24,25}

In addition, in terms of DEM simulation of single particle impact crushing, Ueda et al. studied the disintegration damage of spherical and ellipsoidal particles using DEM. The results indicated that only slender particles can undergo bending fracture.²⁶ Farsi used the Combined Finite Discrete Element Method (FDEM) to study the effect of catalyst carrier shape on its final strength and crushing behavior. The results showed that particle shape, as an inherent characteristic that cannot be ignored, is an important factor determining the multilevel evolution of ore particles during the crushing process.²⁷ Zheng et al. corrected the discrete element fracture model of sand and gravel through one-dimensional compression experiments, and explored the fracture behavior and permeability evolution of 20/40 mesh Jordan fracturing sand using the corrected fracture standards.²⁸ In addition, they also introduced a three-dimensional particle fragmentation model using discrete element numerical simulation methods to represent the fragmentation of proppant particles, and analyzed the effects of reduced particle size distribution and crack closure on the permeability of proppant filling and crack conductivity.²⁹ The

existing literature often utilizes simulation software such as PFC and EDEM to implement DEM simulation. Most of these simulation software require a cumbersome particle modeling process and slow computation for simulating the crushing process. Rocky DEM overcomes these challenges by supporting the import of various intermediate CAD models to establish real particle shapes, making the modeling of particle systems simple and fast. It also has advanced solvers and efficient parallel technology, greatly improving computational speed. In addition, the software also integrates multiple fragmentation models to predict the degree of particle fragmentation, raising the computing power and accuracy to the forefront of the industry.^{6,17,30} Therefore, this article uses Rocky DEM (Rocky DEM 2022 R1.2) software to study the fragmentation distribution characteristics of single particles under rotational impact.

To more precisely analyze the crushing distribution characteristics of the particles and thereby reveal the crushing mechanism of the vertical shaft impact crusher. Drawing inspiration from the crushing principle of the particles in the vertical shaft impact crusher, this study devised a rotary impact tester and established a cumulative damage model of the particle and a simulation model of the crushing system of the rotary impact based on fracture mechanics theory. The crushing process was simulated using various rotor speeds and particle shapes as inputs. Subsequently, an analysis was conducted to determine the impact of rotor speed and particle shape on the crushing distribution characteristics. The impact of rotor speed and particle shape on the particle size distribution of the crushed products is investigated, offering theoretical insights that can inform the design of impact crushers that prioritize energy efficiency, environmental friendliness, and effective crushing operations.

2. DESIGN OF THE EXPERIMENTAL SETUP

A rotary impact testing apparatus is devised in this article in adherence to the vertical shaft impact crusher's crushing principle. The primary operational components of the rotary impact tester comprise the rotor and the crushing chamber, as illustrated in Figure 1. A particle is introduced into the upper cover of the crushing chamber through the inlet. Subsequently, the particle enters the rotor via gravity and is arbitrarily allocated to an accelerating pipeline by the dividing cone. Particles within the accelerating pipeline are propelled along its terminus by centrifugal force. Ultimately, these particles collide with the anvil situated in the crushing chamber, where they are shattered.

The structure of the rotor, which is the fundamental element responsible for accelerating particles, significantly influences the size and velocity of the particles. In conjunction with the specific crushing demands, the rotor's primary structural parameters are devised as follows: rotor height of 80 mm, inlet diameter of 50 mm, rotor diameter of 400 mm, and dividing cone height of 10 mm. The diameter of the four acceleration pipelines is 50 mm. To optimize the crushing effect, the particles accelerated by the rotor must make vertical contact with the anvil to the greatest extent feasible. To accomplish this, the anvil tooth profile is determined using the involute curve.³¹ The crushing chamber's primary structural parameters are formulated as follows: 12 anvils with a diameter of 1200 mm and a spreading angle of 30° for the anvil tooth profile.

3. ESTABLISHMENT OF THE MATHEMATICAL MODEL OF MATERIAL CRUSHING

The material particles in a vertical shaft impact crusher have a polyhedral shape. Crushing occurs within the crushing chamber through contact between edges, surfaces, and points. It is worth noting that this process consumes a significant amount of energy. The normal force contact model permits substantial energy dissipation, and calculating the plastic energy dissipation during particle contact using the lagged linear spring model³² does not necessitate additional simulation time. Consequently, the contact force model is computed in this paper utilizing the linear spring coulomb limit model for the force tangential component and the hysteretic linear spring model for the force normal component. eq 1 computes the current moment normal contact force of particles during the crushing process.

$$F_t^n = \begin{cases} \min(K_{nn}s_n^t, F_n^{t-\Delta t} + K_{nu}\Delta s_n) & \text{if } \Delta s_n \geq 0 \\ \max(F_n^{t-\Delta t} + K_{nu}\Delta s_n, \lambda K_{nn}s_n^t) & \text{if } \Delta s_n < 0 \end{cases} \quad (1)$$

and:

$$\Delta s_n = s_n^t - s_n^{t-\Delta t} \quad (2)$$

where F_t^n and $F_n^{t-\Delta t}$ are the normal contact forces, N, at the current moment and the previous time step, respectively; Δt is the time step, s; Δs is the amount of overlap when the particles are in contact, positive when the particles are close to other particles or the crusher wall, and negative when they are far away; K_{nu} and K_{nn} is the stiffness at impact and impact unloading, respectively, N/m; and λ is a dimensionless constant.

Furthermore, the tangential contact force exerted on the particles can be determined using a linear spring. Limit of coulomb model:

$$F_{\tau,e}^t = F_{\tau}^{t-\Delta t} - K_{\tau}\Delta s_{\tau} \quad (3)$$

where $F_{\tau}^{t-\Delta t}$ is the tangential force, N, on the particle in the last time step; Δs_{τ} is the relative tangential displacement in the time step, mm; and K_{τ} is the tangential stiffness, N/m, calculated as

$$K_{\tau} = r_K K_{nl} \quad (4)$$

where r_K is the tangential stiffness ratio.

In this scenario, the particles are impacted by the tangential force's limiting value, provided that it does not surpass the coulomb limit. Consequently, the complete formulation for the tangential force is

$$F_{\tau}^t = \min(|F_{\tau,e}^t|, \mu F_n^t) \frac{F_{\tau,e}^t}{|F_{\tau,e}^t|} \quad (5)$$

where F_n^t is the contact normal force at time t ; μ is the friction coefficient, defined as

$$\mu = \begin{cases} \mu_s & \text{if no sliding takes place at the contact} \\ \mu_d & \text{if sliding does take place at the contact} \end{cases} \quad (6)$$

where μ_s is the static friction coefficient of the particles; μ_d is the dynamic friction coefficient of the particles.

When the particle breaks, the resulting subparticle fragments preserve both mass and volume in the discrete element

software. Particle fragmentation is primarily detected through the measurement of energy absorbed by the particles during impact.³³ The present study employs the Tavares crushing model to simulate the properties of particles subjected to impact crushing. The crushing model is well-suited for the examination of rock-crushing challenges involving the reduction of particle size in various crusher types.^{2,6,34} The Tavares crushing model posits that each particle possesses a distinct fracture energy.³⁵ This fracture energy is solely determined by the properties of the particle. Breakage of the particles occurs when the impact energy surpasses the fracture energy of the particles. King's research demonstrated that the probability distribution function of particle fragmentation is equivalent to the distribution of fracture energy and is constructed using an upper truncated normal distribution function superimposed on the fracture energy.³⁶

$$\begin{cases} P_0(E) = \frac{1}{2} \left[1 + \operatorname{erf} \left(\frac{\ln E^* - \ln E_{50}}{\sqrt{2\sigma_E^2}} \right) \right] \\ E^* = \frac{E_{\max} * E}{E_{\max} - E} \end{cases} \quad (7)$$

where E^* is the relative specific fracture energy, J/kg; E is the Specific fracture energy, J/kg; E_{50} is the median fracture energy, J/kg; σ_E is the variance of the fracture energy distribution; E_{\max} is the upper cutoff value of the distribution, J/kg.

The equation that represents the median fracture energy of the particles is as follows:

$$E_{50} = E_{\infty} \left[1 + \left(\frac{d_0}{d_p} \right)^{\varphi} \right] \quad (8)$$

where E_{∞} , d_0 , φ is the fitting parameter; d_p is representative particle size contained in size class, mm.

Instances where particles are exposed to an impact energy that falls short of their breaking point result in particle damage, which is physically represented as a decrease in the initial fracture energy. The calculation of the reduced fracture energy is possible via eqs 9 and 10):

$$E_n = E_{n-1}(1 - D_n^*) \quad (9)$$

$$D_n^* = \left(\frac{2\gamma}{(2\gamma - 5D_n^* + 5)} \frac{E_{k,n}}{E_{n-1}} \right)^{2\gamma/5} \quad (10)$$

where E_{n-1} and E_n are the fracture energies of the particles before and after particle impact, J/kg, respectively; D_n^* is the amount of damage to the particle at the n th impact; $E_{k,n}$ is the n th impact energy, J/kg; and γ is the damage constant.

Upon the initial crushing of the particles, the subparticles residual impact kinetic energy will persist in perpetuating the aforementioned crushing process. The quantification of particle fragmentation can be achieved by employing t_{10} :

$$t_{10} = A \left[1 - \exp \left(-b' \frac{E_k}{E_b} \right) \right] \quad (11)$$

where t_{10} is the proportion of subparticles whose size after crushing is less than $L/10$ of the particles before crushing, %; A is the maximum value reached at t_{10} , percent; b is the coefficient of the selection function, kg/J; $E_{k,b}$ is the value of

the specific impact energy at the instant of breakage, J/kg; E_b is a measure of the specific fracture energy of the broken particles, J/kg.

Based on the value of t_{10} , the complete particle size distribution after impact crushing of single particles is given by eq 12:

$$\gamma = 10t_{10} \left(\frac{x}{L} \right) \quad (12)$$

where γ is the cumulative percentage of subparticles, %; x is the screen size, mm; and L is the diameter of the particles before crushing, mm.

The fragmentation process of particles simulated by Rocky DEM is shown in Figure 2, where the blue path represents the

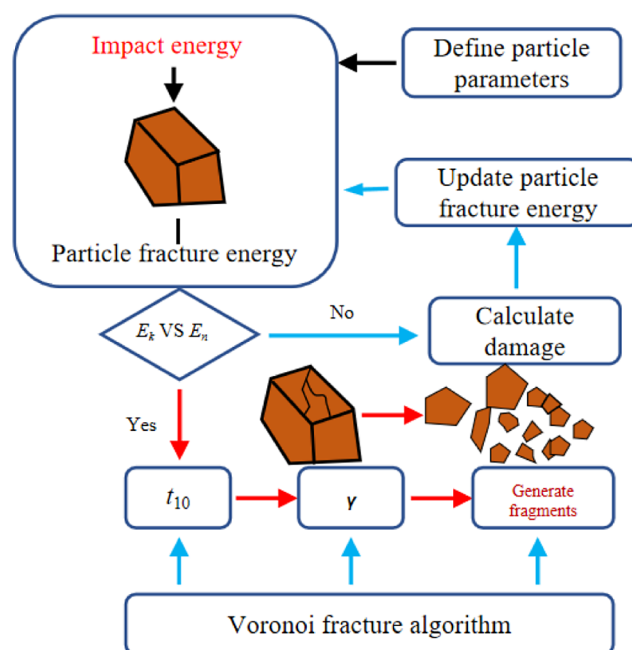







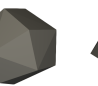

Figure 2. Particle crushing model.

weakening of particles. The red path represents complete fragmentation of particles and their formation into sub particle fragments. First, the relevant material parameters are set. Rocky DEM detects the impact and calculates the absorbed energy E_k in each impact event. Then, the calculated impact energy E_k is compared with the particle fracture energy E_n , which is smaller than the initial fracture energy. Otherwise, the particles undergo complete fragmentation and form sub particle fragments. The degree of particle fragmentation is determined by t_{10} and γ , and the geometric shape of the generated fragments is calculated using Voronoi fracture algorithm.⁶

4. SIMULATION MODELING

4.1. Particle Modeling. To examine the impact of particle shape on the distribution properties of particle impact crushing, this research paper utilizes six distinct particle shapes and three groups of varying rotor speeds to conduct experiments on limestone particles, a material frequently encountered in crushers.³⁷ The particle sizes and shapes are

Table 1. Limestone Particle Shape and Size (Particle Equivalent Diameter of 20 mm)

Particle shape							
Particle Code	Particle 1	Particle 2	Particle 3	Particle 4	Particle 5	Particle 6	Particle 7
Vertical Aspect Ratio (H)	0.5	0.5	0.50	0.50	1.07	1.07	1.07
Horizontal Aspect Ratio (V)	1.76	1.38	1.00	0.50	0.92	0.92	0.92
Surface Number (C)	25	25	25	25	25	15	10
Sphericity	2	2	2	2	2	2	2
Particle mass (kg)	0.0088	0.0069	0.0055	0.0162	0.0090	0.0077	0.0076

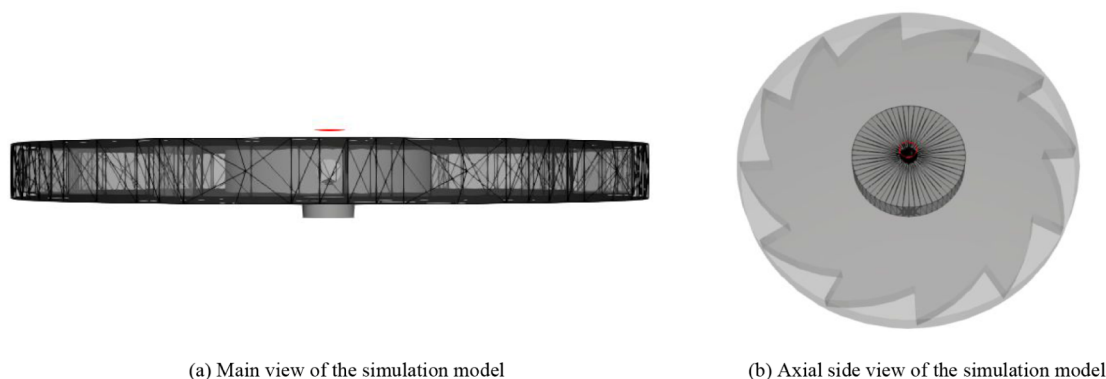


Figure 3. Simulation model of rotational impact tester.

Table 2. Material Parameters and Contact Parameters

material parameters			contact parameters		
physical parameter	limestone	rotary impact tester	physical parameter	limestone–limestone	limestone–tester
Poisson's ratio	0.218	0.28	static friction	0.5	0.6
densities (kg/m ³)	2700	7800	kinetic friction	0.01	0.01
Young's modulus	1.54×10^{10}	2.4×10^{11}	coefficient of restitution	0.1	0.2

Table 3. Limestone Crushing Parameters

crushing parameters	σ_2	E_{max}/E_{50}	E_{∞} (J/kg)	d_0 /mm	φ	γ	A	b
limestone	0.09	4	150	0.79	1.3	5	0.634	0.033

detailed in Table 1. The particle shape was determined using the shape of sand and gravel particles obtained from the crushing site of the vertical shaft impact crusher at Hongjiadu Power Station. This shape was determined using four parameters: the number of facets comprising the particles, the degree of sphericity (the ratio of surface area of a sphere with the same volume as an object to surface area of an object), the horizontal aspect ratio (the ratio of horizontal width to horizontal length of particles), and the vertical aspect ratio (the ratio of vertical height to horizontal length of particles).^{38,39}

4.2. Simulation Modeling of the Test Machine. As illustrated in Figure 3, the simulation model of the simplified rotary crushing test machine is constructed in the Rocky Dem software using the simplified testing machine's structure.

4.3. Setting of Simulation Parameters. Steel is selected for both the rotor and the crushing chamber to simulate the impact crushing of a single particle. The gravitational acceleration was established at 9.8 m/s^2 , the particles' initial velocity was 0.5 m/s , and they were discharged from a distance of 120 mm from the rotor's center. Table 2 presents the particle and contact parameters of the limestone particles as well as the tester.⁴⁰

As shown in Table 3, the parameters of the crushing model for limestone particles were derived by fitting data from single particle impact crushing experiments.^{41,42}

5. RESULTS AND DISCUSSION

5.1. Validation of the DEM Simulation Model. As illustrated in Figure 4, impact crushing experiments were conducted on individual limestone particles using a pneumatic impact test device that was independently designed and fabricated to validate the accuracy of the crushing model. Air compressor, gas tank electric control switch, ball valve, acceleration tube, particle impact chamber, impact plate, light source, high-speed camera, computer, and so forth comprise the experimental apparatus. A particle is introduced into the experiment through the opened ball valve, which is subsequently closed. The particle descends by weight into the accelerating tube, which is filled with high-pressure gas. This causes the particle to strike the steel plate. The high-speed video camera documents the progression of the event. Upon completion of the crushing process, the particles are gathered in the collection box situated at the device's base. This box serves as a repository for the statistics.

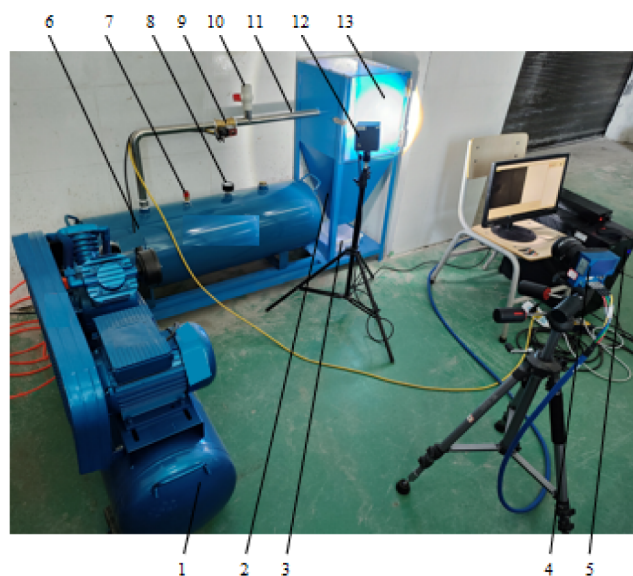
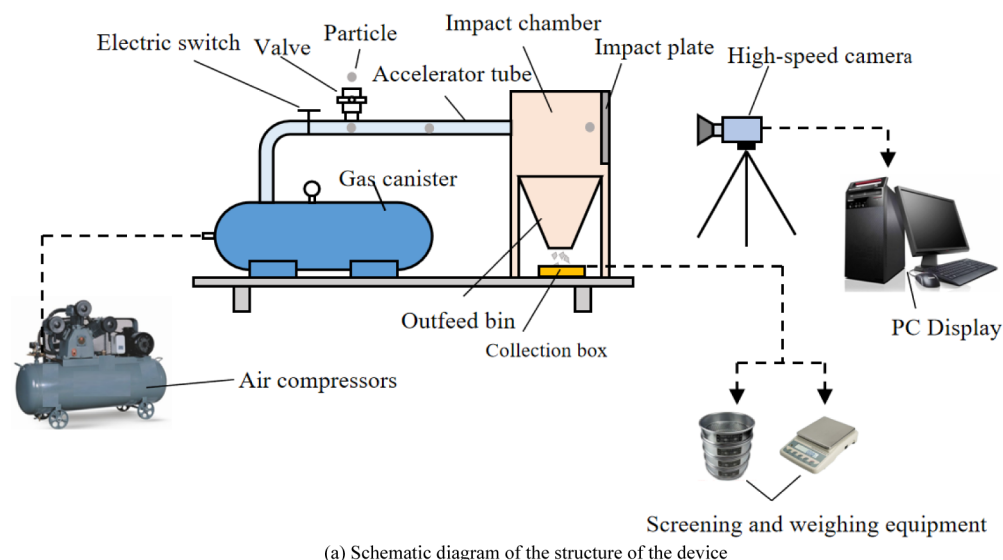


Figure 4. Experimental setup 1. Air compressor 2. High-speed camera 3. Computer 4. Air storage tank 5. Safety valve 6. Pressure gauge 7. Electronic control switch 8. Ball valve 9. Acceleration tube 10. Light source 11. Particle impact chamber.

The impact-crushing process of the particles with the steel plate is documented using a high-speed camera. The impact velocity, morphology, and crushing morphology of the particles after the collision, along with the motion state of the small particles, are derived from each frame of the particle crushing process captured on video by the high-speed camera (see Figure 5a). The formula for determining the impact velocity of particles with the collision plate is

$$v = f_0 L / (N_{f1} - N_{f2}) \quad (13)$$

where v is the impact velocity of the particle, m/s; f_0 is the frame rate of the high-speed camera, f/s; L is the distance from the end of the accelerating tube to the steel plate, $L = 0.2$ m; N_{f1} is the sequence number of the video frames when the particle appears at the end of the accelerating tube; and N_{f2} is the sequence number of the video frames when the particle is in contact with the steel plate.

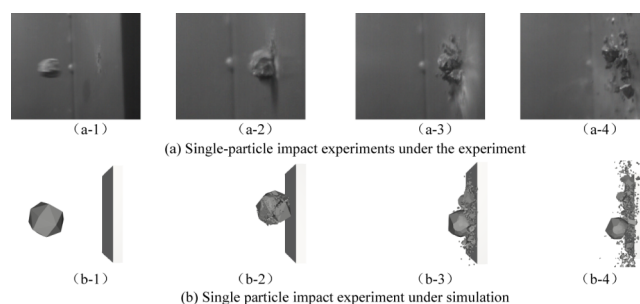


Figure 5. Single-particle impact crushing process.

Figure 5a illustrates that the process of impact-crushing individual particles can be categorized into four distinct stages. Initially, the particles undergo a vertical impact with the steel plate, as illustrated in Figure 5(a-1). Upon impact, cracks initiate to form within the particles, leading to explosive fragmentation, as depicted in Figure 5(a-2). Particles begin

monolithic fragmentation when cracks develop to a certain extent, as depicted in Figure 5(a-3); ultimately, completely broken subparticles scatter in all directions, as illustrated in Figure 5(a-4). eq 12 was utilized to determine the initial velocity of particles ejected during the impact, which is depicted in Figure 5a as 25.2 m/s. Based on the particle grain shape observed in the pneumatic impact crushing experiments, a discrete element model of particles was developed. A simulation test involving a single particle crushing was performed in the crushing test machine simulation model at the same throwing speed; the crushing process of the particles was documented and is depicted in Figure 5b. The crushing morphology of the particles during the experimental and simulated crushing processes is essentially identical, as shown in Figure 5b. This suggests that the established crushing model is reasonably reliable. To validate the simulation model of the crushing system, the particle size distribution of individual particles after the crushing process was quantified, as illustrated in Figure 6. Among them, L is the size of the sieve.

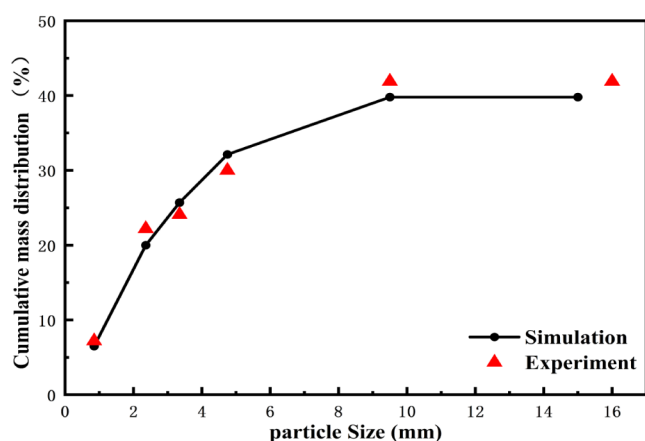


Figure 6. Particle size distribution under simulation and experimentation.

As shown in Table 4, the cumulative mass percentage of each particle size after crushing was determined independently for the single particle impact crushing experiment and simulation test.

Table 4. Cumulative Mass Percentages under Simulation and Experimentation

particle size	test	emulation	relative error
0.85 mm	7.2%	6.5%	9.7%
2.36 mm	22.2%	20%	9.9%
3.35 mm	24.1%	25.7%	6.6%
4.75 mm	30.0%	32.1%	7%
9.5 mm	41.9%	39.8%	5%
maximum particle size (mm)	16	15	

The maximum relative error observed in the cumulative mass percentage for each particle size during the single-particle impact crushing experiment and the simulation test is 9.9%. Furthermore, the discrepancy in the maximum particle size produced is a mere 1 mm, as indicated in Table 4. Thus, the reliability of the crushing system simulation model developed in this paper is substantial.

5.2. Single Particle Impact Crushing Process. Using particle 7 as an example, the established simulation model generates a time-dependent change in the normal stress during the impact crushing of a single particle at a rotor speed of 1000r/min, as depicted in Figure 7. As shown in Figure 8, the

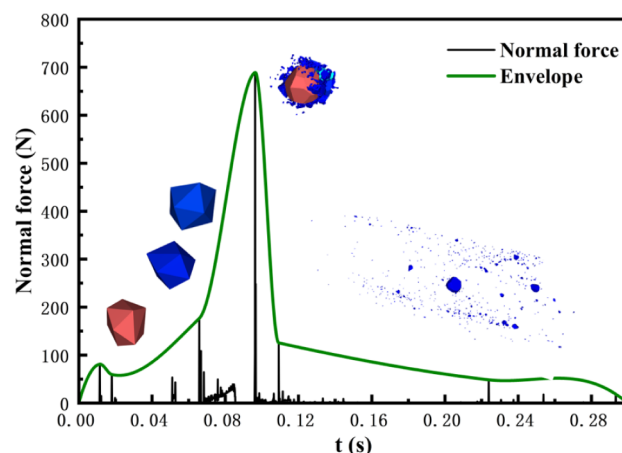


Figure 7. Particle normal stress during rotational impacts.

stress and fragmentation of the particles at various stages of the impact-crushing process were also recorded. The motion position and stress of the particle in the tester at each moment are denoted as (a-1)-(f-1), while the magnified view in the tester is denoted as (a-2)-(f-2). The normal stress on the particles is 0N in the interval 0–0.0115s, as shown in Figure 7. This value, when combined with Figure 8a, indicates that the particles were falling at this time and therefore did not make contact with the testing machine. The particles' normal stress fluctuates and reaches 80.9 N at $t = 0.0115$ s. When viewed in conjunction with Figure 8b, it is evident that the particles make contact with the rotor and that the impacts on the particles result primarily from the transformation of the particles' gravitational potential energy; however, these impacts do not attain the threshold for particle crushing, and thus the particles are not crushed. The normal force on the particles varies between 0.0115 and 0.848s, reaching a peak value of 176.5 N. Particles are accelerated in the rotor and subjected to constant impacts from the rotor wall during this period, as illustrated in Figure 8c. As illustrated in Figure 8d, the particles are propelled along the termination of the acceleration pipe at $t = 0.848$ s due to the rotor's acceleration. The particle experiences a maximum normal force of approximately 688.9 N at time $t = 0.963$ s. Upon exiting the rotor and undergoing a collision with the anvil, the particle is currently undergoing holistic crushing, as illustrated in Figure 8e. The observed maximum normal force at time $t = 0.100$ s is approximately 91.3 N. As shown in Figure 8f, this is because the subparticle fragments maintain contact with the anvil edge as a result of the secondary impact energy that remains after the anvil strikes. The normal force exerted on the particles gradually diminishes to zero beyond $t = 0.100$ s. This signifies that the fragments of the broken particles eventually return to rest, depleting any remaining impact energy. In addition, the energy dissipation of particles 7 during the crushing process is approximately 456.738J/kg.

Rocky Dem performed postprocessing on the data. The resulting diameter distribution pattern of the crushed subparticles was computed and is depicted in Figure 9. The particle size distribution characteristics of particles 7 after

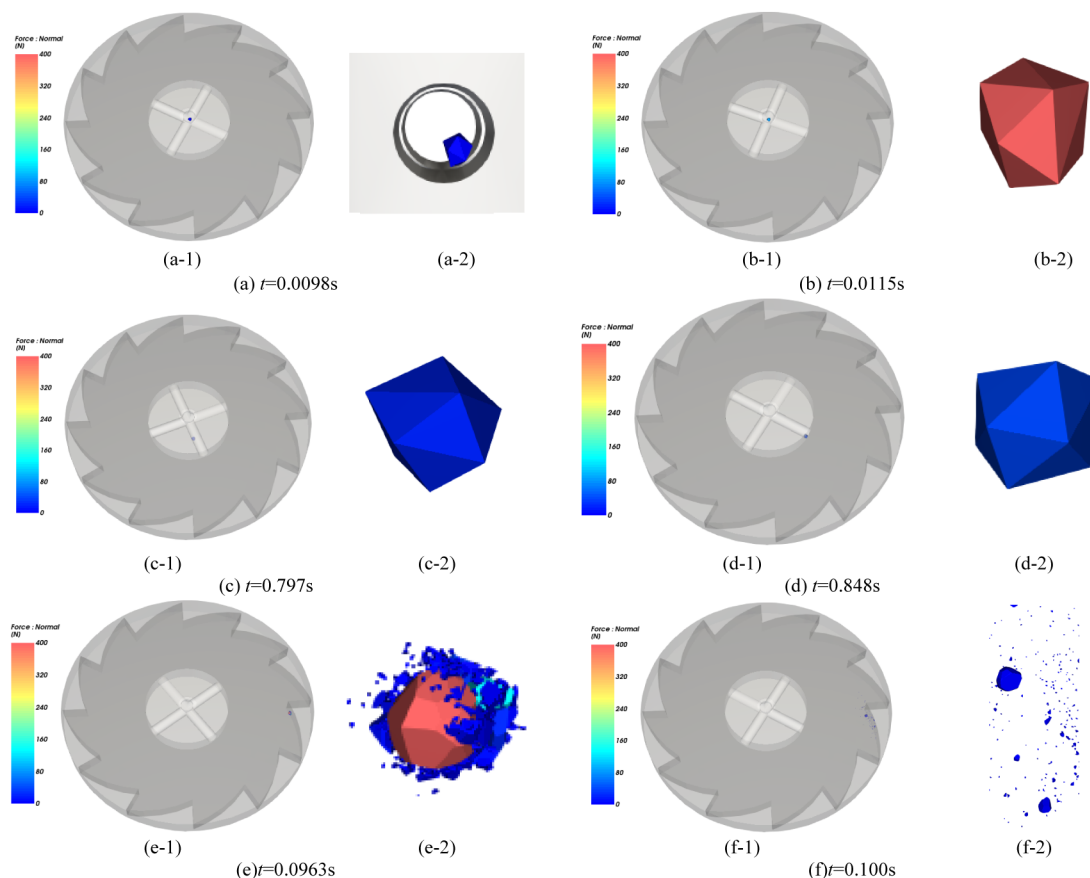


Figure 8. Particle rotational impact crushing process (particles are colored by normal force magnitude).

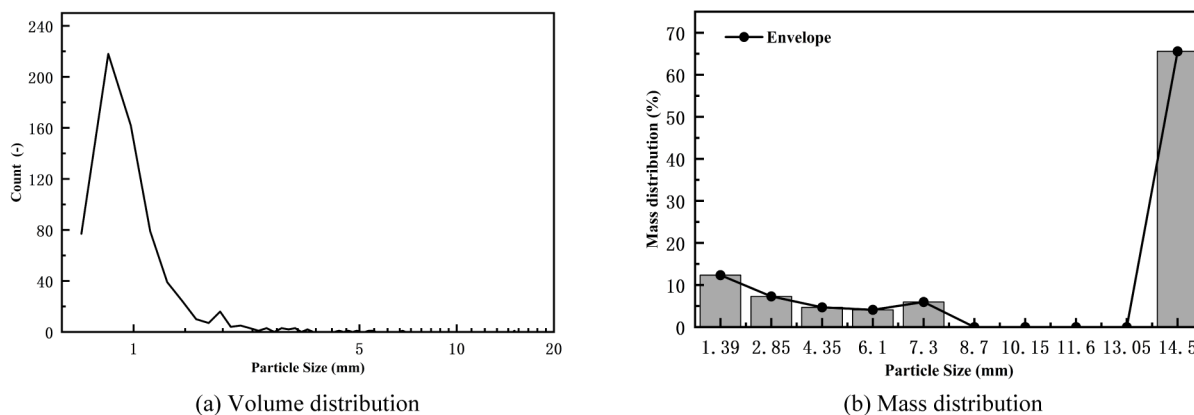


Figure 9. Particle size distribution of single-particle crushed products.

crushing were also presented in Figure 9. 664 subparticles are generated as a result of impact crushing a solitary particle, as illustrated in Figure 9a. The subparticle diameters exhibited a high degree of concentration within the range of less than 2 mm. The number of subparticles surpassing 2 mm was relatively small. The particle size distribution of the subparticles was characterized by a single peak, with a mean value near 0.8 mm. Merely 1–2 particles within the subparticles possessed a diameter exceeding 10 mm. As shown in Figure 9b, the mass distribution of single particles following crushing was also computed; the average mass percentage for each particle size is represented by the gray bar chart. When viewed in conjunction with Figure 9a,b

demonstrates that the particles with larger diameters maintain a greater mass distribution, comprising 70% of the total mass, although only 1–2 particles in the subparticles have a diameter greater than 10 mm. This is due to the positive correlation between particle mass and diameter. The aforementioned findings suggest that single-particle impact crushing generates one subparticle with a significant diameter and a substantial quantity of particles with a smaller diameter.

5.3. Effect of Rotor Speed on Impact Crushing Characteristics. As representatives, particles 3, 5, and 6 were chosen based on their characteristic particle shapes. The purpose of this analysis was to simulate and examine the impact crushing distribution at rotor speeds of 1000 r/min,

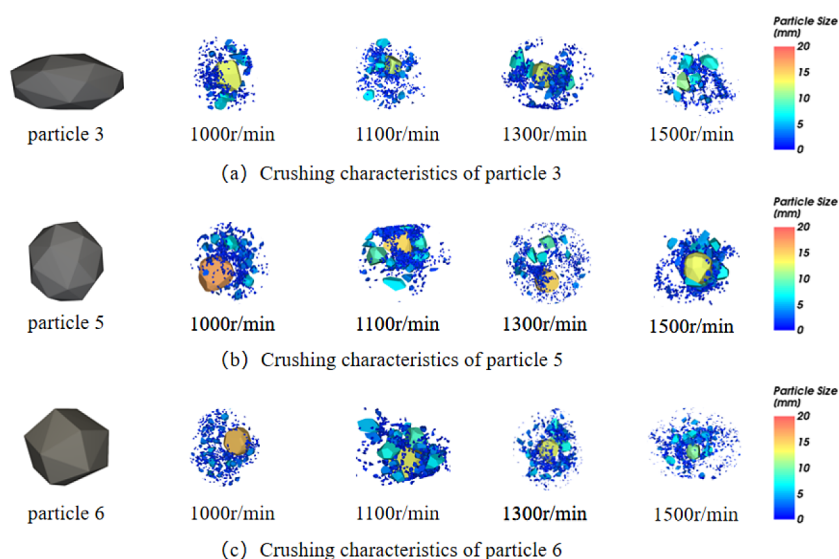


Figure 10. Particle impact crushing characteristics (particles are colored according to their size).

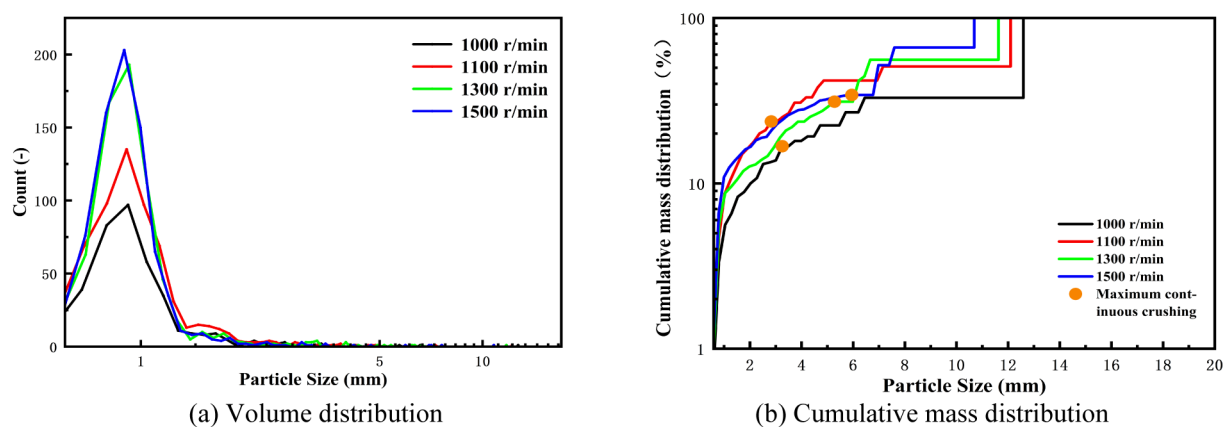


Figure 11. Particle 3 crushing characteristics.

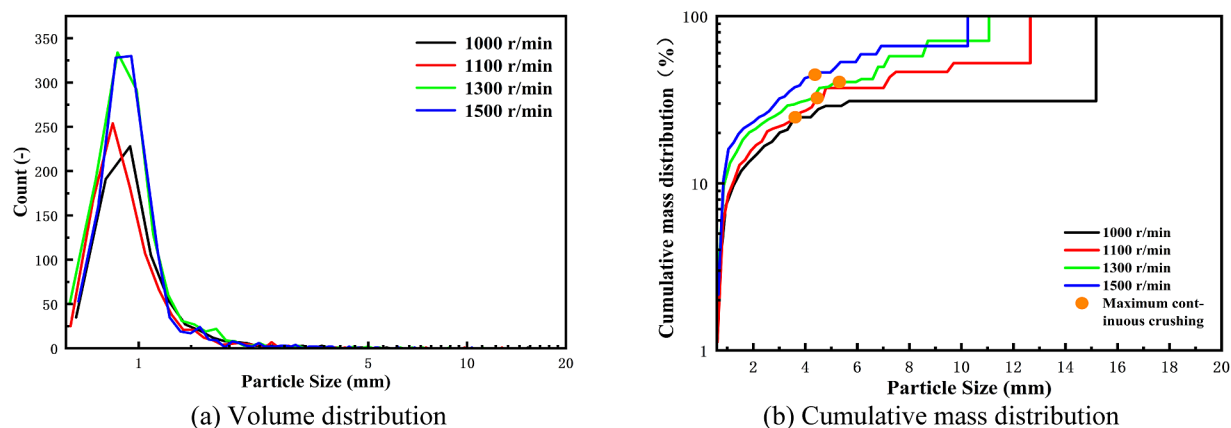


Figure 12. Particle 6 fragmentation characteristics.

1100 r/min, 1300 r/min and 1500 r/min, respectively. The fragmentation distribution of individual particles after concealing the rotor and crushing chamber is illustrated in Figure 10. The color blocks on the right-hand side represent the diameter of the fragmented subparticles. As illustrated in Figure 10, as rotor speed increases, subparticles generated by individual particles become more minute.

Particles 3 ($V = 1$) and 6 ($C = 15$) were subjected to impact crushing, as illustrated in Figure 10a,c. Particles 3 and 6 undergo substantial changes in their distribution characteristics as the rotor speed increases, resulting in the formation of a substantial quantity of smaller subparticles. Nevertheless, it is evident from Figure 10b that particle 5 possesses distinct distribution characteristics in comparison to particles 3 and 6.

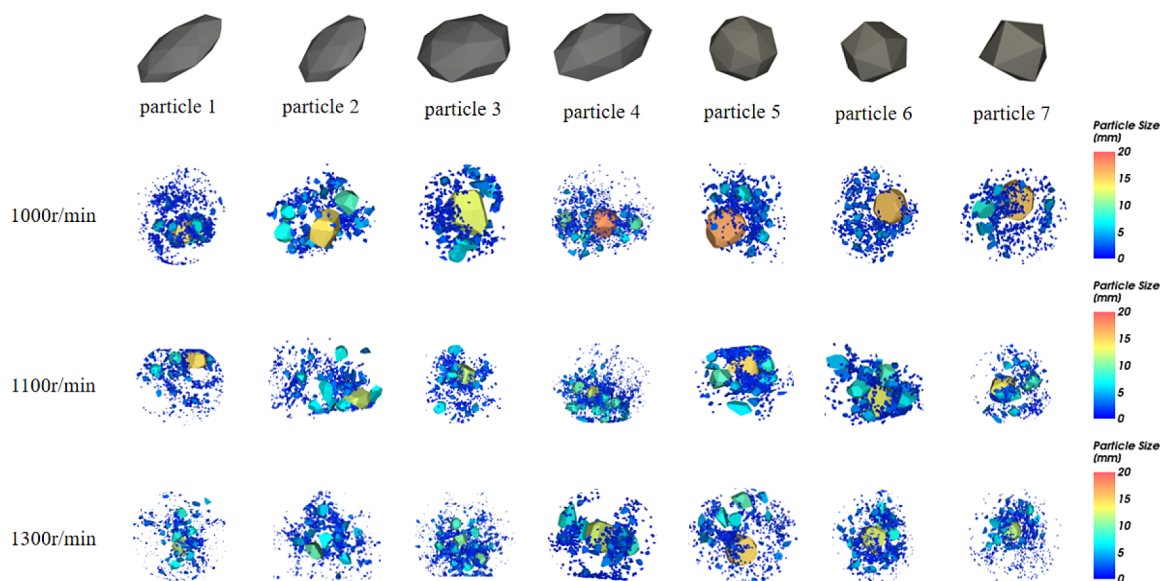


Figure 13. Particle impact crushing characteristics (particles are colored according to their size).

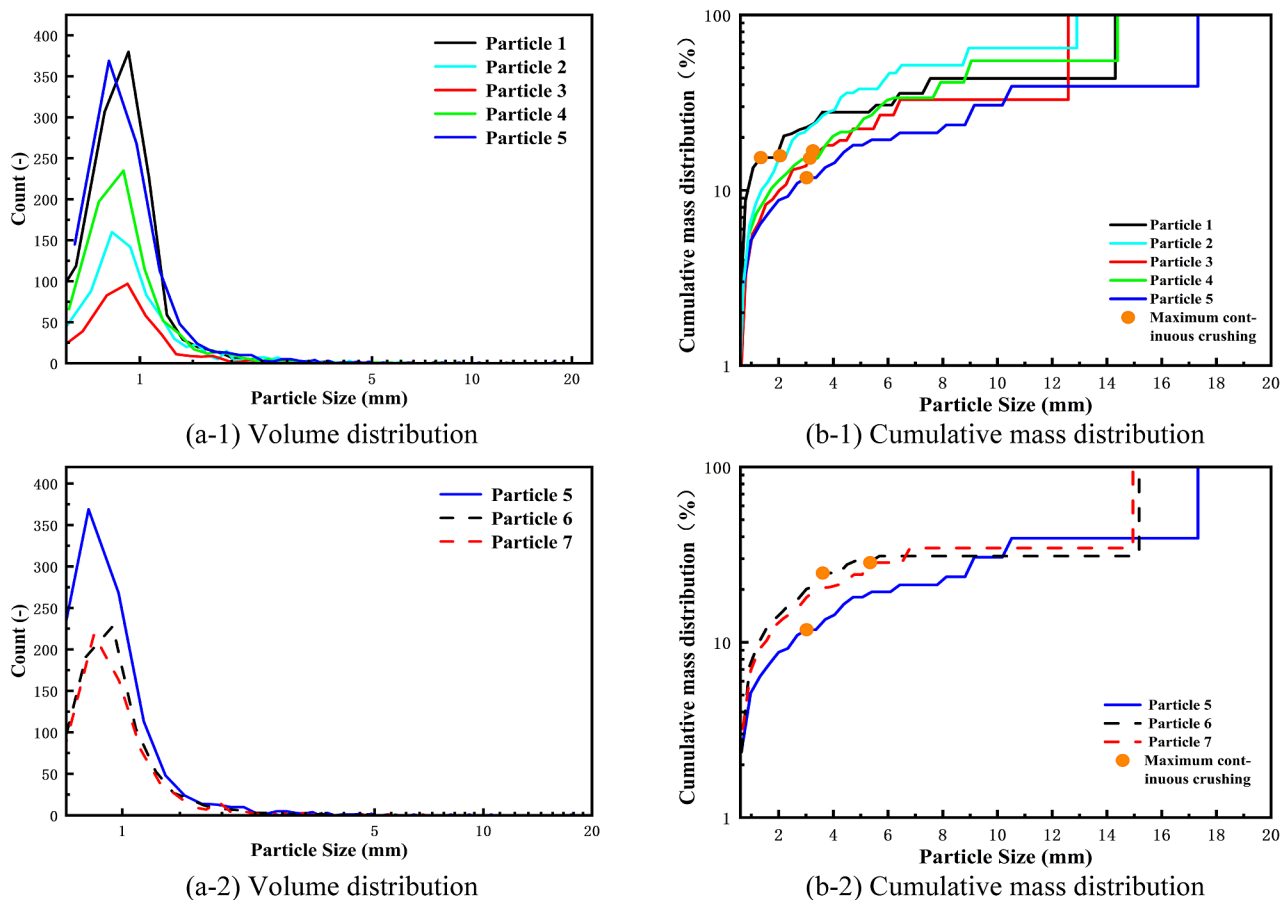


Figure 14. Crushing characteristics (1000r/min).

While the rotor speed does cause an increase in the number of subparticles comprising particle 5, the subparticles that are crushed exhibit a more substantial particle size. The impact lumpiness distribution characteristics indicate that spherical particles 5 are more difficult to break than ellipsoidal particles 3 and particles 6 featuring sharp edges.

Furthermore, a quantitative analysis was conducted to determine the impact of rotor speed on the crushing distribution characteristics of particle 3. As shown in Figure 11, the particle size distribution curve of particle 3 was initially computed. The relationship between particle size and the number of subparticles is illustrated in Figure 11a, while the cumulative mass is depicted in Figure 11b. It is evident from

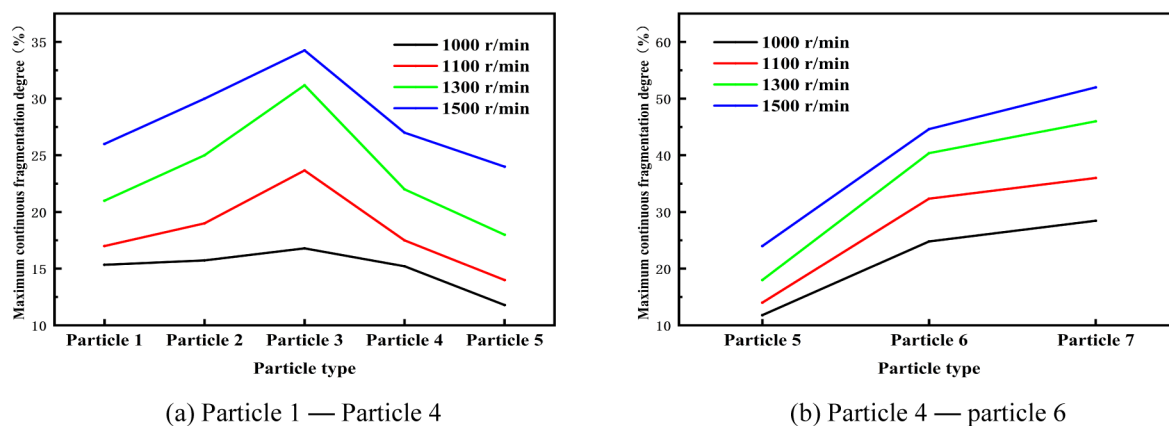


Figure 15. Maximum continuous fragmentation of particles.

Figure 11a that the quantity of subparticles remaining following particle crushing is reduced when the rotor speed reaches 1000 rpm. This phenomenon is represented by a single peak distribution. The gradual increase in the peak value as the rotor speed reaches 1300 rpm is since as the rotor speed rises, so does the impact energy of the particles and the quantity of subparticles generated through particle impact crushing. Furthermore, it can be observed from Figure 11b that as the rotor speed increases, the maximum continuous crushing mass of the ellipsoidal-shaped particles 3 also increases.

Particle 6 with sharp edges is fragmented as depicted in Figure 12. Likewise, as shown in Figure 12a, the number of subparticles increases substantially as rotor speed increases. In contrast to the particle 3 crushing scenario, an alteration in rotor speed from 1000 to 1100 rpm results in a leftward shift of the subparticle size distribution peak and the generation of subparticles characterized by reduced diameters. This is because the subparticles retain a significant amount of impact energy even after being crushed, causing them to undergo additional crushing in the testing machine. When considering Figure 12b, it becomes evident that as rotor speed increases, the maximum continuous crushing mass of particle 6 also continues to rise.

5.4. Influence of Particle Shape on Impact Crushing Characteristics. To investigate the influence of particle shape on impact crushing, six established particle models were chosen. The particles had an equivalent diameter of 20 mm. To simulate the crushing distribution characteristics of the particles in the rotary impact experiment, a rotating test machine simulation model was implemented. The simulation outcomes are illustrated in Figure 13, with the color blocks on the right side representing the diameter size of the subparticles.

As illustrated in Figure 13, when the rotational speed is 1000 rpm, the subparticles generated by the crushing of particle 5 have the largest diameter in comparison to particles 1, 2, 3, and 4. This conclusion is drawn based on an examination of the particle shapes. As the horizontal aspect ratio of the particles (particle 1- particle 3) increases, the diameter of the largest subparticle generated through impact crushing diminishes in the crushing pattern of oblate ellipsoidal particles. The diameter of the largest subparticle generated through impact crushing, on the other hand, increases gradually in long ellipsoidal particles with increasing horizontal aspect ratios (particle 3-particle 5). When particles 5, 6, and 7 were compared, it was observed that the subparticle generated from particle 5 with the greatest diameter was the largest.

Furthermore, as the particle edges become more pronounced (particle 5-particle 7), there is a gradual reduction in the diameter of the largest subparticle generated through impact crushing. Under various rotational velocities, the impact of particle shape on the size distribution of crushed subparticles exhibits a consistent pattern.

Using, as an illustration, the impact crushing effect at 1000r/min rotor speed, Figure 14 computes the crushing distribution patterns of seven different types of particles. As illustrated in Figure 1(a-1) and Figure 1(b-1), the quantity of subparticles generated through crushing is reduced when the rotor speed is set to 1000 rpm. This is because particle 3 has a smaller mass and volume, assuming the equivalent diameter of the particles remains constant. Nevertheless, according to the cumulative mass distribution curve, particle 3 has the most cumulative mass from the continuous crushing of the five particles. Particle 5 has the smallest maximum continuous crushing cumulative mass among the particles; this is indicated by the gradual decrease in maximum continuous crushing cumulative mass when V is less than one and V is greater than one. Similarly, the particle size distribution and cumulative mass distribution of particles with progressively sharper angles (particle 5-particle 7) are depicted in Figure 14 (a-1) and Figure 14 (b-2). Due to the relatively small mass and volume of particles 6 and 7 in comparison to particles 5, the number of subparticles generated through the process of crushing is minimal. As a result of the progressively sharper edges of the particle prongs, the maximum subparticle diameters and overall subparticle diameters produced by the fragmentation of particle 7 and particle 6 are relatively small. The cumulative maximum crushing mass of the particles experiences an upward trend as the sharpness of their edges increases.

5.5. Trends in Maximum Continuous Crushing Degree. In contrast to substantial particle quantity crushing, continuous crushing, and other crushing methods, the particle size distribution of subparticles generated through impact crushing of individual particles is comparatively narrower and less continuous, exhibiting a discernible degree of discreteness. Following impact crushing of particles of various shapes, the cumulative mass of the subparticles exhibited step characteristics. The degree of particle crushing in the rotary impact experiment is significantly influenced by both the initial particle shape and the impact energy.

The faster the rotor speed, the more the subparticle sizes resulting from single-particle fragmentation are concentrated in a continuous interval, and therefore the higher the degree of

particle fragmentation.³³ To facilitate the assessment of the extent of fragmentation exhibited by individual particles, the degree of fragmentation can be quantified using eq 14, which represents the ratio of the cumulative mass of the subparticles during the maximum continuous interval to the total mass of the particles:

$$\eta = m_i/M \quad (14)$$

where η is the maximum continuous crushing degree of particles; m_i is the total mass of the subparticles in the maximum continuous interval, kg; M is the total mass of the particles, kg. The maximum continuous crushing degree after impact crushing of single particles of different shapes was counted according to eq 13, as shown in Figure 15.

It is evident from Figure 15a,b that the maximum continuous crushing degree increases as rotor speed increases for particles of the same shape, and the trend is consistent. Additionally, the variation trend of the maximum continuous crushing degree for particles 1, 2, 3, 4, and 5 exhibits an inverted "V" shape as the horizontal aspect ratio V of the particles increases, as depicted in Figure 15a. In particular, the maximum continuous fragmentation of particles exhibits a gradual decrease for values of V that are less than one and greater than one. Furthermore, the maximum continuous fragmentation is the smallest for particles approaching spherical morphology, suggesting that extreme ellipsoidal and spherical particles are the most challenging to fragment. The maximum continuous crushing degree of particles 5, 6, and 7 is depicted in Figure 15b. The maximum continuous crushing degree increases as the edges of the particles become progressively sharper; this indicates that the edges of the particles become more pronounced, which contributes to the crushing process.

6. CONCLUSION

Based on the theory of fracture mechanics, a model of cumulative particle damage resulting from repeated impacts was developed. The discrete element model of various single particle shapes and the simulation model of the rotary impact crushing test machine were developed following the crushing principle of the vertical shaft impact crusher. The following conclusions were reached after employing quantitative and qualitative analysis techniques to examine the impact of various rotor speeds and grain shapes on the rotary impact crushing properties of single particles:

The form of particle crushing within the tester was ascertained through the examination of the crushing process and the normal stress of a solitary particle.

As the rotor speed was elevated, the particle size distributions of subparticles generated through impact crushing of particles featuring various particle shapes exhibited singular-peak properties, with the peak value progressively augmenting. Furthermore, as rotor speed increases, so do the cumulative mass distribution curve and the maximum continuous crushing cumulative mass.

When the horizontal aspect ratio of particles is less than 1 or greater than 1, the crushing effect of particles remains inadequate at the same rotational speed. However, as the edges of particles become progressively sharper, the crushing effect improves.

The maximum continuous crushing degree of the particles exhibited an inverted "V" shape as the horizontal aspect ratio

of the particles increased; the sharp edges of the particles contributed to the maximum continuous crushing degree.

AUTHOR INFORMATION

Corresponding Author

Limei Zhao – School of Mechanical Engineering, Guizhou University, Guiyang 550025, China; orcid.org/0009-0009-3886-3358; Email: lmzhao@gzu.edu.cn

Authors

Canhui Wu – School of Mechanical Engineering, Guizhou University, Guiyang 550025, China

Zhen Cao – School of Mechanical Engineering, Guizhou University, Guiyang 550025, China

Complete contact information is available at:

<https://pubs.acs.org/10.1021/acsomega.4c00997>

Funding

This work was financially supported by the National Natural Science Foundation of China (no. 52065007).

Notes

The authors declare no competing financial interest.

REFERENCES

- (1) Al-Khasawneh, Y. Novel design modeling for vertical shaft impactors. *Powder Technol.* **2024**, *433*, 119205.
- (2) Al-Khasawneh, Y. Development and testing of a novel mathematical-physical model for the design of ring armor for the vertical shaft impact crushers. *Miner. Eng.* **2021**, *170* (1–2), 106994.
- (3) Segura-Salazar, J.; Barrios, G. P.; Rodriguez, V.; Tavares, L. M. Mathematical modeling of a vertical shaft impact crusher using the Whiten model. *Miner. Eng.* **2017**, *111*, 222–228.
- (4) Numbi, B. P.; Xia, X. Optimal energy control of a crushing process based on vertical shaft impactor - ScienceDirect. *Appl. Energy* **2016**, *162*, 1653–1661.
- (5) Fang, H.; Yang, J.; Song, Y.; Huang, W.; Chen, J. Simulation and experimental study on the stone powder separator of a vertical shaft impact crusher - ScienceDirect. *Adv. Powder Technol.* **2020**, *31* (3), 1013–1022.
- (6) Atamanuk, K.; Thomas, M. C.; Wadams, R. C.; Linthicum, W.; Yu, W.; Huey, B. D. Atomic Force Microscopy to Identify Dehydration Temperatures for Small Volumes of Active Pharmaceutical Ingredients. *Powder Technol.* **2020**, *360*, 1271–1277.
- (7) Subero, J.; Ghadiri, M. Breakage patterns of agglomerates. *Powder Technol.* **2001**, *120* (3), 232–243.
- (8) Yu, F. W.; Zhao, C.; Liu, W. C. On single particle breakage behavior of crushable weathered sands. *J. Mt. Sci.* **2022**, *19*, 3627–3644.
- (9) Zhou, B.; Wei, D.; Ku, Q.; Wang, J.; Zhang, A. Study on the effect of particle morphology on single particle breakage using a combined finite-discrete element method. *Comput. Geotech.* **2020**, *122*, 103532.
- (10) Samimi, A.; Ghadiri, M.; Boerefijn, R.; Groot, A.; Kohlus, R. Effects of Structural Characteristics on Impact Breakage of Agglomerates. *Powder Technol.* **2003**, *130*, 428–435.
- (11) Zeng, Y.; Jia, F.; Xiao, Y.; Han, Y.; Meng, X. Discrete element method modelling of impact breakage of ellipsoidal agglomerate. *Powder Technol.* **2019**, *346*, 57–69.
- (12) da Cunha, E. R.; Cavalcanti, P. P. S.; Saeidi, F.; Marcelo Tavares, L. On the limitation of using the JKRB in investigating incremental breakage. *Miner. Eng.* **2018**, *118*, 33–36.
- (13) Tavares, L. M. Analysis of particle fracture by repeated stressing as damage accumulation. *Powder Technol.* **2009**, *190* (3), 327–339.
- (14) Tavares, L. M.; King, R. P. Modeling of particle fracture by repeated impacts using continuum damage mechanics. *Powder Technol.* **2002**, *123* (2), 138–146.

- (15) Tavares, L. M.; King, R. P. Single-particle fracture under impact loading. *Int. J. Miner. Process* **1998**, *54*, 1–28.
- (16) Faruk, S.; Musaffa Ayyşen, L. One-dimensional compression behavior of granular soils around virgin compression line (VCL). *Bull. Eng. Geol. Environ.* **2023**, *82*, 227.
- (17) Bengtsson, M.; Evertsson, C. M. Measuring characteristics of aggregate material from vertical shaft impact crushers. *Miner. Eng.* **2006**, *19* (15), 1479–1486.
- (18) Zheng, K.; Du, C.; Li, J.; Qiu, B.; Fu, L.; Dong, J. Numerical simulation of the impact-breakage behavior of non-spherical agglomerates. *Powder Technol.* **2015**, *286*, 582–591.
- (19) Wang, W.; Coop, M. R. An investigation of breakage behaviour of single sand particles using a high-speed microscope camera. *Géotechnique* **2016**, *66*, 984–998.
- (20) Golshan, S.; Sotudeh-Gharebagh, R.; Zarghami, R.; Mostoufi, N.; Blais, B.; Kuipers, J. A. M. Review and Implementation of CFD-DEM Applied to Chemical Process Systems. *Chem. Eng. Sci.* **2020**, *221*, 115646.
- (21) Huang, Z.; Lin, X.; Chen, C. Fast Texture Synthesis for Discrete Example-based Elements. *IEEE Access* **2020**, *8*, 76683–76691.
- (22) Benedetto, M. F.; Borio, A.; Scialò, S. Mixed Virtual Elements for discrete fracture network simulations. *Finite Elem. Anal. Des.* **2017**, *134*, 55–67.
- (23) Liu, H.-Z.; Lin, J.-S.; He, J.-D.; Xie, H.-Q. Radom Discrete Elements and Size Effects. *Eng. Fract. Mech.* **2018**, *189*, 246–272.
- (24) Luo, Z.; Ye, C.; Xiao, H.; Yin, J.; Liang, Y.; Ruan, Z.; Luo, D.; Gao, D.; Tan, Q.; Li, Y.; et al. Optimization of loop-mediated isothermal amplification (LAMP) assay for robust visualization in SARS-CoV-2 and emerging variants diagnosis. *Chem. Eng. Sci.* **2022**, *251*, 117430.
- (25) Gawenda, T.; Saramak, D. Researchers from AGH University of Science and Technology Detail Research in Mineral Research (Optimization of Aggregate Production Circuit through Modeling of Crusher Operation). *Mining & Minerals Daily* **2022**, *12*, 78. (Feb.8).
- (26) Ueda, T.; Matsushima, T.; Yamada, Y. DEM simulation on the one-dimensional compression behavior of various shaped crushable granular materials. *Granular Matter* **2013**, *15*, 675–684.
- (27) Farsi, A.; Xiang, J.; Latham, J. P.; Carlsson, M.; Stitt, E. H.; Marigo, M. Strength and fragmentation behaviour of complex-shaped catalyst pellets: A numerical and experimental study. *Chem. Eng. Sci.* **2020**, *213*, 115409.
- (28) Zheng, W.; Hu, X.; Tannant, D. D. Shape Characterization of Fragmented Sand Grains via X-Ray Computed Tomography Imaging. *Int. J. Geomech* **2020**, *20* 3
- (29) Zheng, W.; Tannant, D. D. Influence of proppant fragmentation on fracture conductivity - Insights from three-dimensional discrete element modeling. *J. Pet. Sci. Eng.* **2019**, *177*, 1010–1023.
- (30) Guo, J.; Wang, G.; Sun, G.; Wang, S.; Guan, W.; Chen, Z. DEM simulation and optimization of crushing chamber shape of gyratory crusher based on Ab-t10 model. *Miner. Eng.* **2024**, *209*, 108606.
- (31) Mu, S.; Zhao, Y.; Zhang, X.; Meng, Q.; Li, G. Meshing theory of involute worm drive. *Mechanism And Machine Theory* **2021**, *165*, 104425.
- (32) Walton, O.; Braun, R. L. Viscosity, Granular-Temperature, and Stress Calculations for Shearing Assemblies of Inelastic, Frictional Disks. *J. Rheol.* **1986**, *30*, 949–980.
- (33) Zhang, S.; Yan, S.; Lu, K.; Qiu, S.; Chen, X. D.; Wu, W. D. Spray freeze dried niclosamide nanocrystals embedded dry powder for high dose pulmonary delivery. *Powder Technol.* **2023**, *415*, 118168.
- (34) Gürsoy, S.; Güzel, E. Technology, Determination of Physical Properties of Some Agricultural Grains. *Res. J. Appl. Sci. Eng.* **2010**, *2* (5), 492–498.
- (35) Tavares, L. M. Chapter 1 Breakage of Single Particles: Quasi-Static. In *Handbook of Powder Technology*; Elsevier 2007, 368 .
- (36) King, R. P.; Bourgeois, F. Measurement of fracture energy during single-particle fracture. *Miner. Eng.* **1993**, *6* (4), 353–367.
- (37) Ceresoli, G.; Chacartegui, R.; Silva, P.; Carro, A.; Ortiz, C.; Becerra Villanueva, J. A. Modelling of a Solid Particle Receiver for Tes and Tces Exploiting Sand and Limestone. Available at SSRN 4355242. 2023. .
- (38) Zheng, W.; Tannant, D. D. Grain breakage criteria for discrete element models of sand crushing under one-dimensional compression. *Comput. Geotech.* **2018**, *95*, 231–239.
- (39) Zheng, W.; Hu, X.; Tannant, D. D.; Zhang, K.; Xu, C. Characterization of two- and three-dimensional morphological properties of fragmented sand grains. *Eng. Geol.* **2019**, *263*, 105358.
- (40) Wu, C.; Zhao, L.; Cao, Z. Collision Energy Analysis within the Vertical Shaft Impact Crusher Based on the Computational Fluid Dynamics-Discrete Element Method. *ACS Omega* **2024**, *9*, 7967–7975.
- (41) Weerasekara, N. S.; Powell, M. S.; Cleary, P. W.; Tavares, L. M.; Evertsson, M.; Morrison, R. D.; Quist, J.; Carvalho, R. M. The contribution of DEM to the science of comminution. *Powder Technol.* **2013**, *248*, 3–24. (Complete)
- (42) Carvalho, R. M. D.; Tavares, L. M. Predicting the effect of operating and design variables on breakage rates using the mechanistic ball mill model. *Miner. Eng.* **2013**, *43-44* (s 43–44), 91–101.